Partitioning the contributions of dependent offshore forcing conditions in the probabilistic assessment of future coastal flooding

Jeremy Rohmer[1], Deborah Idier[1], Remi Thieblemont[1], Goneri Le Cozannet[1], François Bachoc[2]

[1] BRGM, 3 av. C. Guillemin, 45060 Orléans Cedex 2, France

[2] Institut de Mathématiques de Toulouse, 118 Rte de Narbonne, 31400 Toulouse, France

Correspondence to: Jeremy Rohmer (j.rohmer@brgm.fr)

Abstract. Getting a deep insight into the role of coastal flooding drivers is of high interest for the planning of adaptation strategies for future climate conditions. Using global sensitivity analysis, we aim to measure the contributions of the offshore forcing conditions (wave/wind characteristics, still water level and sea level rise (*SLR*) projected up to 2200) to the occurrence of a flooding event at Gâvres town on the French Atlantic coast in a macrotidal environment. This procedure faces, however, two major difficulties, namely (1) the high computational time costs of the hydrodynamic numerical simulations; (2) the statistical dependence between the forcing conditions. By applying a Monte-Carlo-based approach combined with multivariate extreme value analysis, our study proposes a procedure to overcome both difficulties by calculating sensitivity measures dedicated to dependent input variables (named Shapley effects) using Gaussian process (GP) metamodels. On this basis, our results show the increasing influence of *SLR* over time, and a small-to-moderate contribution of wave/wind characteristics, or even negligible importance in the very long term (beyond 2100). These results were discussed in relation to our modelling choices, in particular the climate change scenario, as well as the uncertainties of the estimation procedure (Monte Carlo sampling and GP error).

1 Introduction

Coastal flooding is generally not caused by a unique physical driver, but by a combination of them, including mean sea-level changes, atmospheric storm surges, tides, waves, river discharges, etc. (e.g., Chaumillon et al., 2017). The intensity of surge itself depends on atmospheric pressure and winds as well as on the site-specific shape of shorelines and water depths (bathymetry). Hence, compound events, resulting from the co-occurrence of two or more extreme values of these processes is a significant reason for concern regarding adaptation. For example, flood severity is significantly increased by the co-occurrence of extreme waves and surges at a number of major tide gauge locations (Marcos et al., 2019), of high sea-level and high river discharge in the majority of deltas and estuaries (Ward et al., 2018), of high sea-level and rainfall at major US cities (Wahl et al., 2015). This intensification of compound flooding is expected to be exacerbated under climate change (Bevacqua et al., 2020). A deeper knowledge of coastal flooding drivers is thus a key element for the planning of adaptation strategies such as engineering, sediment-based or ecosystem-based protection, accommodation, planned retreat, or avoidance (Oppenheimer et al., 2019); see also discussion by Wahl (2017).

In this study, we analyse compound coastal flooding at Gâvres town on the French Atlantic coast. This site has been impacted by 4 major coastal flooding events since 1905 (Idier et al., 2020a); in particular, by the storm event Johanna on March 10, 2008, which resulted in about 120 flooded houses (Gâvres mayor: personal communication; Idier et al., 2020a). Flooding processes at this site are known to be complex (macro tidal regime and wave overtopping; variety of natural and human coastal defences, various exposure to waves due to the complex shape of shorelines); see a thorough investigation by Idier et al. (2020a). We aim to unravel which offshore forcing conditions among wave characteristics (significant wave height, peak period, peak direction), wind characteristics (wind speed at 10m, wind direction) and still water level (combination of mean sea-level, tides and atmospheric surges) drive severe compound flood events, considering projected sea-level rise (*SLR*), up to 2200.

We adopt here a probabilistic approach to assess flood hazard, i.e. we aim to compute the probability of flooding and to quantify the contributions of the drivers with respect to the occurrence of the flooding event by means of global sensitivity analysis, denoted GSA (Saltelli et al., 2008). This method presents the advantage of exploring the sensitivity in a global manner by covering all plausible scenarios for the inputs' values and by fully accounting for possible interactions between them. The method has been applied successfully in different application cases in the context of climate change (e.g., Anderson et al., 2014; Wong et al., 2017; Le Cozannet et al., 2015; 2019a; Athanasiou et al. 2020).

Unlike these previous studies, the application of GSA to our study site faces two main difficulties: (1) the physical processes related to flooding are modelled with numerical simulations that have an expensive computational time cost (i.e. larger than the simulated time). This hampers the Monte-Carlo-based procedure for estimating the sensitivity measures; (2) the offshore forcing conditions cannot be considered independent and the probabilistic assessment should necessarily account for their statistical dependence. This complicates the decomposition of the respective contributions of each physical drivers in GSA (see a discussion by Do and Razavi, 2020).

Our study proposes a procedure to overcome both difficulties by combining multivariate extreme value analysis (Heffernan and Tawn, 2004; Coles, 2001) with advanced GSA techniques specifically adapted to handle dependent inputs (Iooss and Prieur, 2019) and probabilistic assessments (Idrissi et al., 2021). To overcome the computational burden of the procedure, we adopt a metamodelling approach, i.e. we perform a statistical analysis of existing databases of pre-calculated high-fidelity simulations to construct a costless-to-evaluate statistical predictive model (named "metamodel" or "surrogate") to replace the long running hydrodynamic simulator; see e.g., Rohmer et al. (2020).

The article is organized as follows. Sect. 2 describes the test case of Gâvres, the data and the numerical hydrodynamic simulator used to assess flood hazard. In Sect. 3, we describe the overall procedure to partition the uncertainty contributions of dependent offshore forcing conditions for future coastal flooding. The procedure is then applied to Gâvres and results are analysed in Sect. 4 for future climate conditions. In Sect. 5, the influence of different scenario assumptions in addition to the offshore forcing conditions is further discussed, namely the magnitude of the flooding events, the influence of the climate change scenario, the digital elevation model (DEM) used as input of the hydrodynamic numerical model, and the intrinsic stochastic character of the waves.

2 Case study

2.1 Numerical modelling of flooding

The considered case study corresponds to the coastal town of Gâvres on the French Atlantic coast in a macrotidal environment (mean spring tidal range: 4.2m). Since 1864, more than ten coastal flooding events hit Gâvres (Le Cornec et al., 2012). The flooding modelling is based on the non-hydrostatic phase-resolving model SWASH (Zijlema et al., 2011), which allows simulating wave overtopping and overflow. The implementation and validation on the study site is described in (Idier et al., 2020a), and we summarize here the main aspects. The computational domain as well as the Digital Elevation Model (DEM) are shown in Fig. 1 (red domain). The DEM (denoted DEM 2015) is representative of the 2015 local bathymetry and topography and of the 2018 coastal defences. The space and time resolution are respectively 3m in horizontal, 2 layers along the vertical dimension, and more than 10Hz. The offshore wave conditions (south of Groix island) are propagated to the boundaries of the SWASH model using the spectral wave model WW3 (Ardhuin et al., 2010) taking into account the local tide, atmospheric surge and wind (see large spatial domain in Fig. 1(a)). The combined WW3-SWASH model chain has been validated with respect to the area that was flooded during the Johanna storm event (which occurred on 10 March 2008): the model slightly overestimates the number of flooded houses by about 3%, which can be considered very satisfactory for such complex environments.
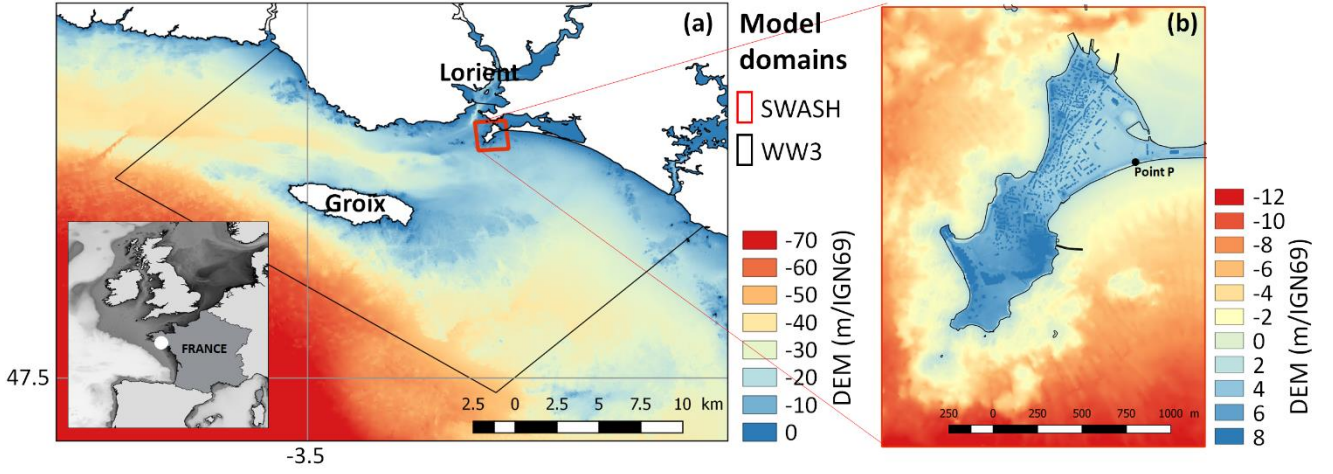
Figure 1: Digital Elevation Model (DEM) and computational domain of the study site of Gâvres for the spectral wave model WW3 (a), and for the non-hydrostatic phase-resolving model SWASH (b). The insert in (a) provides the regional setting. The point P indicates an observation point on the coast. Adapted from Idier et al. (2020a).

The inland impact of a storm event is assessed by estimating the total water volume Y that has entered the territory at high tide. This is performed by first running the WW3 model (over 2 hours to reach steady wave conditions), and then the SWASH model by considering a time span of 20 minutes (with 5 minutes spin up) and steady state offshore forcing conditions. The value of Y is the volume at the end of the simulation. Such simulation costs about 1h30 of time computation on 48 cores approximately. Fig. 2 provides the maps of water depth and the corresponding value of Y computed with the afore-described simulator for five different storm events. In the study, we use the volume value $Y=50\text{m}^3$, $2,000\text{m}^3$ and $15,000\text{m}^3$ to categorize the flooding event as "minor", "moderate" and "very large". In addition, to account for the random character of waves, the modelling of the coastal flood induced by overtopping processes is combined with a random generation of wave characteristics in SWASH as described by Idier et al. (2020b). For given offshore forcing conditions, the simulation is repeated $n_r=20$ times, and the median value (denoted m_Y) of Y is calculated. The impact of wave stochasticity is further discussed in Sect. 5.1.
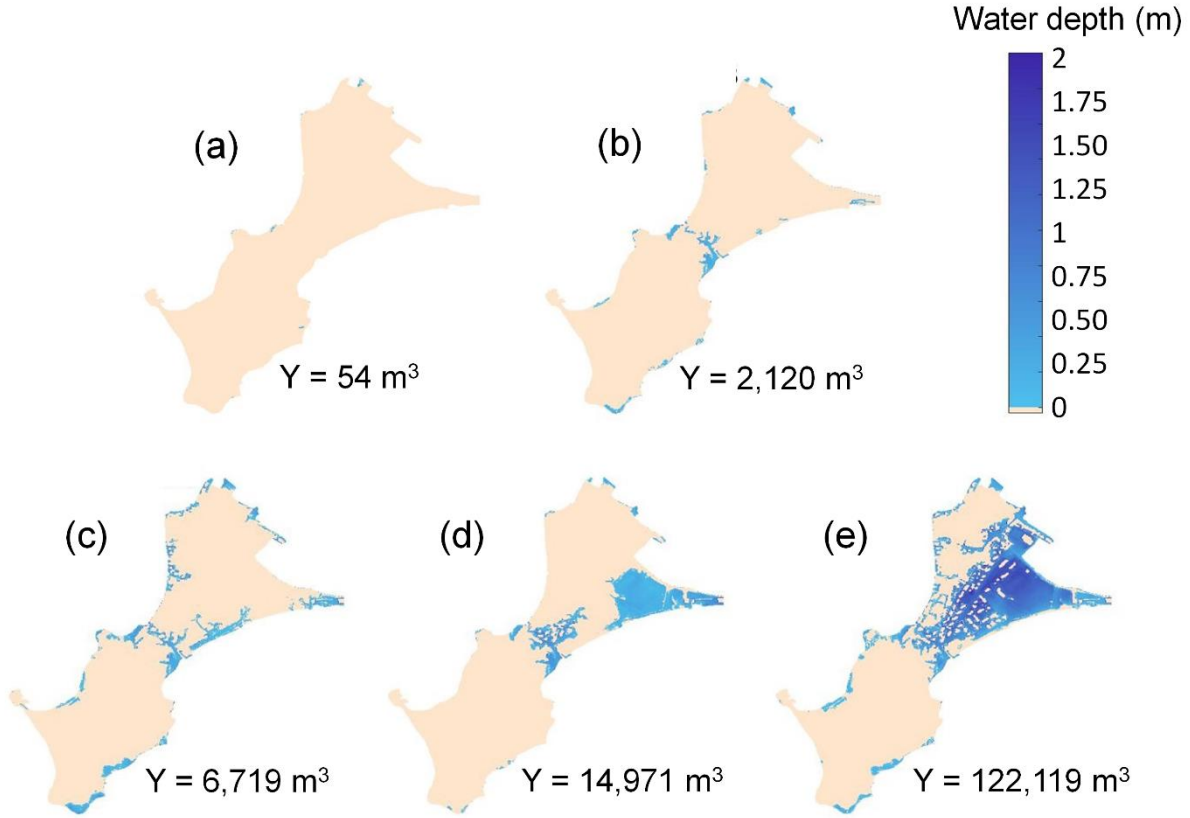
Figure 2: Examples of five maps of water depth modelled by the numerical simulator described in Sect. 2 using DEM 2015. The value of the flood-induced inland water volume Y is indicated for the five cases. In the study, the volume value 50m³, 2,000m³ and 15,000m³ have been selected to categorize the flooding event as minor, moderate and very large. Note that due to lack of numerical results with Y close to 15,000m³ in the database of simulation results (see Sect. 5), map (d) is provided for DEM 2008 instead.

2.2 Offshore forcing conditions

The modelling chain is forced by six offshore conditions, namely the still water level (*SWL*) – expressed with respect to the mean sea level, the significant wave height (*Hs*), the peak period (*Tp*), the direction (*Dp*), the wind speed at 10m (*U*) and wind direction (*Du*). These are defined using a database composed of hindcasts of past conditions offshore of the study site over the period 1900-2016. This dataset was built via the concatenation of hindcasts of different sources (see Idier et al., 2020a: Table 1 for further details) completed by bias corrections using a quantile-quantile correction method. A total of >80,000 past events characterized by sixplets (*SWL, Hs, U, Tp, Dp,* and *Du*) taken at the time instant of the high tide, are used in the following to constrain the statistical methods of Sect. 3. The visual analysis of the extracted conditions (black dots in Fig. 3) suggests a moderate-to-large statistical dependence between the forcing conditions, because we can clearly see a structure between the points: if they were independent, no structure would be noticed. The analysis of the pairwise Pearson's correlation highlights a high and statistically significant correlation coefficient of 62% and of 50% for (*Hs*, *U*) and (*Hs*, *Tp*) respectively. In addition, the examination of the extremal dependence using the summary statistics described by Coles et al. (1999) shows that (*SWL, Hs, U*) present statistically significant positive dependence in the class of asymptotic independence (ranging between 28 and 46%). Further details are provided in Supplementary Materials A.
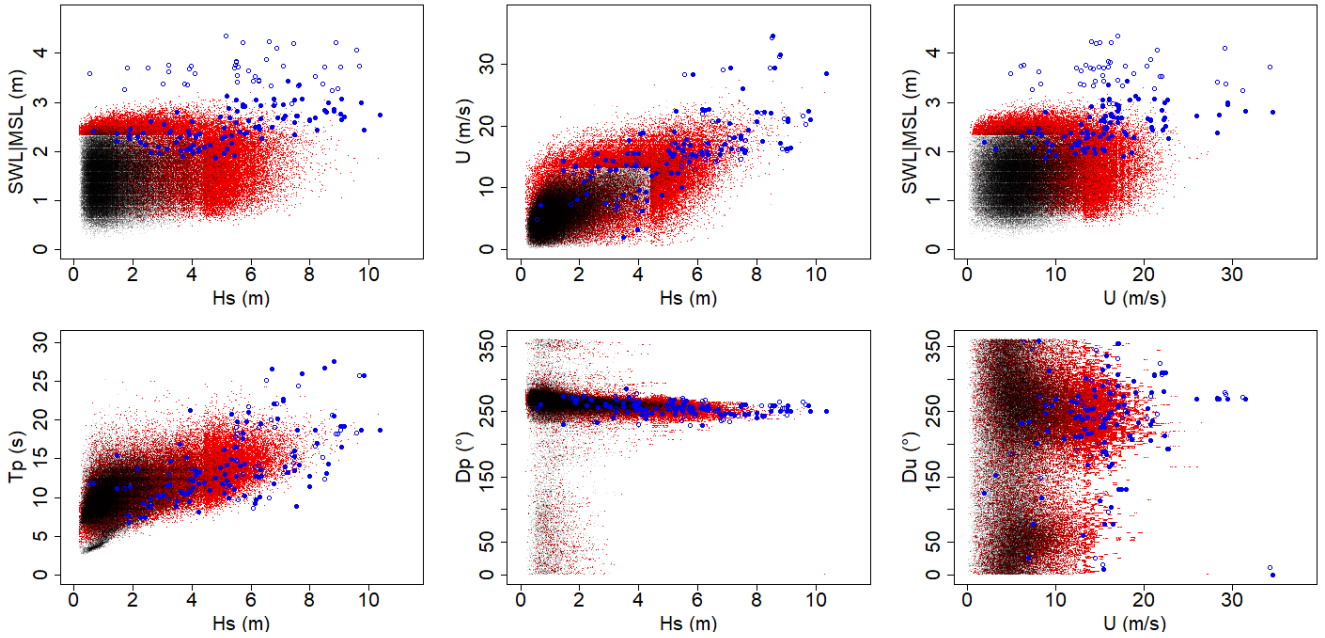
115 **Figure 3: Overview of the N=50,000 randomly generated samples of offshore conditions (red dots). Black dots correspond to the hindcast conditions used to fit the statistical methods described in Sect. 3.3. Blue (open and filled) circles correspond to the n=144 training data used to set-up the GP metamodel (the selection approach is detailed in Sect. 3.2). The open circles correspond to cases that are deliberately selected outside the range of the red dots to cover a broader range of situations.**

2.3 Sea level projections

120 The analysis is conducted for future climate conditions by computing future still water level as $SWL_f(t) = SLR^{RCP}(t) + SWL$, where $SLR^{RCP}(t)$ is the value of local mean sea level change in the future (relative to a given reference date) for a given a climate change scenario, i.e. a RCP (Representative Concentration Pathway) scenario, and SWL is the present day still water level expressed with respect to the mean sea level of the considered reference date.

In this study, we use the $SLR^{RCP}(t)$ projections provided by Kopp et al. (2014) in the vicinity of the study site (including **125** corrections of vertical ground motion of -0.25 +/- 0.16 mm/y). These projections and associated uncertainty were based on a combination of expert community assessment (the IPCC-AR5), expert elicitation (e.g., Bamber and Aspinall, 2013), and process modelling (e.g., the 5th phase of the Coupled Model Intercomparison Project or CMIP5) for most sea-level contributors, i.e. thermal expansion and ocean dynamical changes, ice-sheet melting, glaciers melting and groundwater storage changes. The data are provided with reference date 2000 for five time horizons (2030, 2050, 2100, 2150 and 2200), for 33 **130** percentile levels p_{SLR} and for three RCP scenarios (RCP2.6, RCP4.5 and RCP8.5). The values for intermediate time instants as well as percentile levels are obtained via interpolation (linear for percentile levels, and kriging-based (Williams and Rasmussen, 2006) for time horizons).

In summary, time-series of SLR^{RCP} are defined by combining a RCP scenario with a percentile level p_{SLR} (ranging between 0 and 1). Fig. 4 shows the projections for the three RCP scenarios considering p_{SLR}=50% (median in red) and $p_{SLR} = 5$ and 95% **135** (90% interval in blue). To account for the uncertainty of SLR^{RCP}, the following random sampling procedure is proposed: (1) a percentile level p_{SLR} is randomly and uniformly sampled between 0 and 1; (2) the inverse cumulative distribution function estimated from the data by Kopp et al. (2014) is then used to sample a time series of projected $SLR^{RCP}(t)$ values for a given RCP scenario, i.e. the same p_{SLR} level is considered over the period 2030-2200 (with a time step of 10 years). See some examples in Fig. 4 of random realisations following this procedure.

140
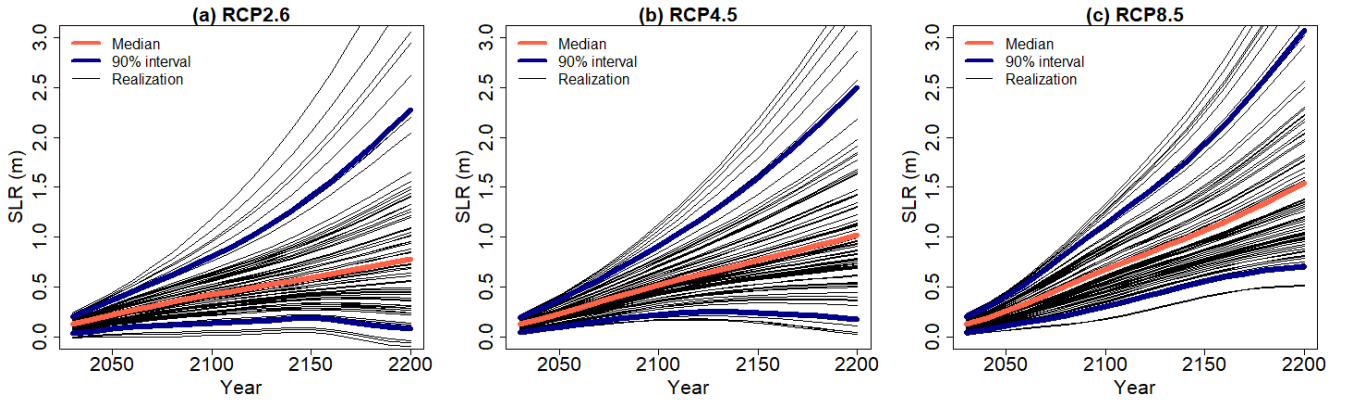
Figure 4: Future projection of regional *SLR* for 3 different RCP scenarios. The red line indicates the median, and the blue lines indicate the bounds of the 90% confidence interval provided by Kopp et al. (2014). The different black lines correspond to a subset of 75 randomly generated time series using the procedure described in Sect. 2.3.

3 Statistical methods

3.1 Overall procedure

The objective is twofold. First, we aim to estimate the flooding probability P_f defined as the probability that the median value m_Y (related to wave stochasticity, see Sect. 2.1) of the inland water volume Y induced by the flood exceeds a given threshold Y_C, namely:

$$P_f = \text{Prob}(m_Y > Y_C) = \text{E}\big(\text{I}_{\{m_Y > Y_C\}}\big) = \text{E}\big(\text{I}_{\{f^{(n_r)}(\mathbf{x}) > Y_C\}}\big) \tag{1}$$

where E(.) is the expectation operator, $\text{I}_{\{A\}}$ is the indicator function which takes up 1 if A is true and 0 otherwise, and $f^{(n_r)}(.)$ denotes the hydrodynamic simulator f(.) described in Sect. 2 which takes the vector $\mathbf{x}$ of offshore forcing conditions as inputs to compute m_Y by conducting $n_r{=}20$ repeated numerical simulations. Second, we aim to quantify the contributions of each offshore forcing conditions to the occurrence of the flooding event defined by $\{m_Y > Y_C\}$. The different steps of the procedure are depicted in Fig. 5 and described below.
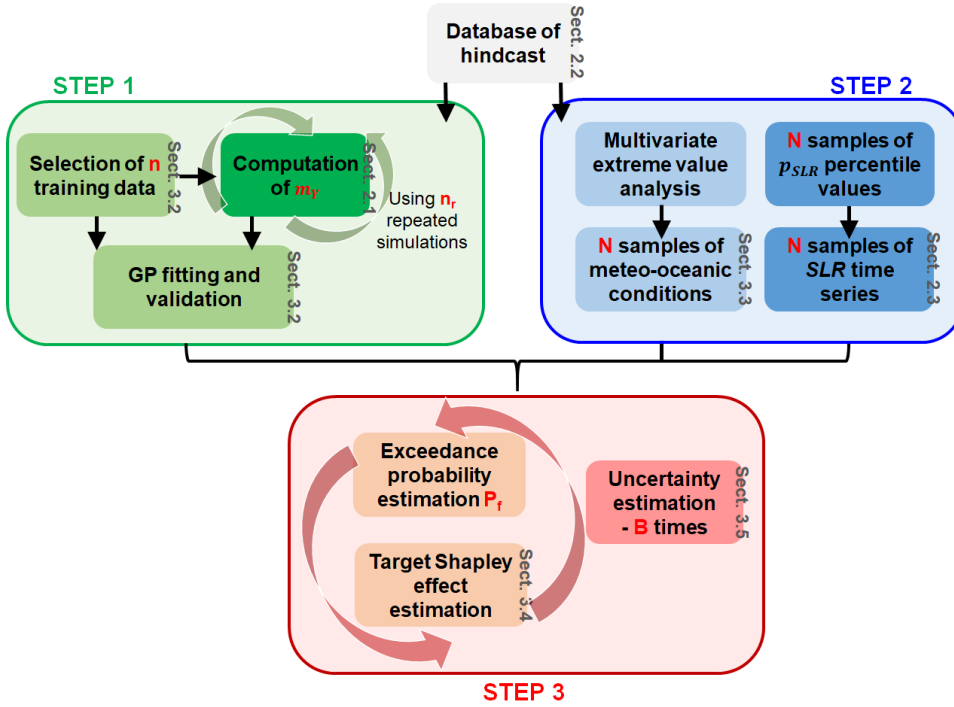
Figure 5: Flowchart of the procedure. The sections describing the methods/data are indicated in grey next to the boxes.

Step 1. To overcome the large computation time cost to estimate m_Y, we set up a metamodel (see details in Sect. 3.3) which is trained using a number n of inputs $\mathbf{x}^{i=1,\dots,n}$ and the corresponding median value $m_Y^i = f^{(n_r)}(\mathbf{x}^i)$ (computed by running the hydrodynamic simulator n_r times). As metamodel, we opt for the Gaussian process (GP) regression method (Williams and Rasmussen, 2006) whose implementation and validation are described in Sect. 3.2. One advantage of GP is to be capable to account for the metamodel error, i.e. the uncertainty related to the approximation of the true numerical model by a metamodel that is built using only a finite number of simulation results (see Step 3);

Step 2. Using the database of hindcasts described in Sect. 2.2, a multivariate extreme value analysis is conducted to randomly generate a large number N of "extreme-but-realistic" random realisations $\mathbf{x}$ of the scalar offshore meteo-oceanic conditions via a Monte-Carlo procedure (Sect. 3.3). The effect of *SLR* is accounted for by following the random procedure described in Sect. 2.3;

Step 3. Using the validated GP metamodel, P_f is estimated using the N randomly generated realisations of the offshore conditions. The respective contribution of the different offshore forcing conditions to the occurrence of the flooding event $\{m_Y > Y_C\}$ is quantified using the tools of GSA (Sect. 3.4). We account for two sources of uncertainty in the estimation procedure, namely the Monte-Carlo sampling, and the GP error by replicating B times the estimation within a Monte-Carlo-based approach described in Sect. 3.5.

3.2 Step 1. Gaussian Process Metamodel

Let us consider the set of n training data $(\mathbf{x}^i, m_Y^i = f^{(n_r)}(\mathbf{x}^i))_{i=1,\dots,n}$. In the context of GP modelling (also named as kriging, Williams and Rasmussen, 2006), we assume, prior to any numerical model run, that $f^{(n_r)}(.)$ is a realisation of a GP $(M_Y(\mathbf{x}))$ with

- mean (also named trend) $\mu(\mathbf{x}) = \sum_{j=1}^{k} \beta_j g_j(\mathbf{x})$ (where g_j are fixed basis functions, and β_j are the regression coefficients of the k input variables);

- stationary covariance function $k(.,.)$, (named kernel) written as $\forall \mathbf{x}, \mathbf{x}', k(\mathbf{x}, \mathbf{x}') = \text{cov}(M_Y(\mathbf{x}), M_Y(\mathbf{x}'))$ with σ^2 the variance parameter.

For new offshore forcing conditions $\mathbf{x}^*$, the predictive probability distribution $M_Y(\mathbf{x}^*) | \{M_Y(\mathbf{x}^1) = m_Y^1, \dots, M_Y(\mathbf{x}^n) = m_Y^n\}$ follows a GP with mean $\mu_{GP}(\mathbf{x}^*)$ and variance $V(\mathbf{x}^*)$ defined using the universal kriging equations (e.g. Roustant et al., 2012) as follows:

$$\mu_{GP}(\mathbf{x}^*) = \mathbf{g}(\mathbf{x}^*)'\hat{\boldsymbol{\beta}} + \mathbf{c}(\mathbf{x}^*)'.\mathbf{C}^{-1}.(\mathbf{m}_Y - \mathbf{G}\hat{\boldsymbol{\beta}}), \tag{2a}$$

$$V(\mathbf{x}^*) = V_S + (\mathbf{g}(\mathbf{x}^*)'\hat{\boldsymbol{\beta}} - \mathbf{c}(\mathbf{x}^*)'.\mathbf{C}^{-1}.\mathbf{G})'.(\mathbf{G}'.\mathbf{C}^{-1}.\mathbf{G})^{-1}.(\mathbf{g}(\mathbf{x}^*)'\hat{\boldsymbol{\beta}} - \mathbf{c}(\mathbf{x}^*)'.\mathbf{C}^{-1}.\mathbf{G}), \tag{2b}$$

where $\mathbf{m}_Y = (M_Y(\mathbf{x}^1) = m_Y^1, \dots, M_Y(\mathbf{x}^n) = m_Y^n)$, $\mathbf{C}$ is the covariance matrix between the points $M_Y(\mathbf{x}^1),\dots,M_Y(\mathbf{x}^n)$ whose element is $C[i,j] = k(\mathbf{x}^i, \mathbf{x}^j)$; $\mathbf{c}(\mathbf{x}^*)$ is the vector composed of the covariance between $M_Y(\mathbf{x}^*)$ and the points $M_Y(\mathbf{x}^1),\dots, M_Y(\mathbf{x}^n)$; $\mathbf{g}(\mathbf{x}^*)$ is the vector of trend functions values at $\mathbf{x}^*$, $\mathbf{G} = (g(\mathbf{x}^1), \dots, g(\mathbf{x}^n))'$ is the experimental matrix, the best linear estimator $\hat{\boldsymbol{\beta}}$ of $\boldsymbol{\beta}$ is $(\mathbf{G}'\mathbf{C}^{-1}\mathbf{G})^{-1}\mathbf{G}'\mathbf{C}^{-1}\mathbf{m}_Y$, and $V_S = \sigma^2 - \mathbf{c}(\mathbf{x}^*)'.\mathbf{C}^{-1}.\mathbf{c}(\mathbf{x}^*)$ by assuming $k(.,.)$ to be stationary (Williams and Rasmussen, 2006).

The n numerical experiments used to train the GP model are selected by combining two techniques: (1) for the extreme values, we use the approach developed by Gouldby et al. (2014) by means of a clustering algorithm applied to a large dataset of extreme forcing conditions. This database is constructed through a combination of Monte Carlo random sampling and multivariate extreme value analysis performed on the database of hindcast conditions described in Sect. 2.2; (2) for low and moderate values, we use the conditioned latin hypercube sampling procedure of Minasny and McBratney (2006). The reader can refer to Rohmer et al. (2020) for further details on the implementation for the site of interest here.

To validate the assumption of replacing the true numerical simulator by the kriging mean (Eq. 2a), we measure whether the GP model is capable of predicting "yet-unseen" input configurations, i.e. samples that have not been used for training. This can be examined by using a K-fold cross-validation approach (e.g. Hastie et al., 2009: Sect. 7.10). To do so, the training data is first randomly split into K roughly equal-sized parts. For the kth part, we fit the GP model to the other K−1 parts of the data, and calculate the prediction error of the fitted model when predicting the kth part of the data. We do this for k = 1,2,...,K and combine the K estimates of prediction error as follows.

Let us consider $\Lambda:\{1,...,n\} \to \{1,...,K\}$ an indexing function that indicates the partition's index to which each data point (of the training dataset) is allocated by randomization, and denote by $\widehat{m}_Y^{-k}(\boldsymbol{x})$ the prediction at $\boldsymbol{x}$ using the GP model fitted using the kth part of the data removed. Then, the cross-validation estimate of the coefficient of determination denoted Q^2 holds as follows:

$$Q^2 = 1 - \frac{\sum_{i=1}^{i=n}\left(m_Y^i - \widehat{m}_Y^{-\Lambda(i)}(x_i)\right)^2}{\sum_{i=1}^{i=n}\left(m_Y^i - \bar{m}\right)^2}, \qquad (3)$$

where m_Y^i is the ith median value of Y computed using the modelling procedure of Sect. 2, and $\bar{m}$ is the average value of the numerically computed median values. A coefficient Q^2 close to 1.0 indicates that the GP model is successful in matching the new observations that have not been used for the training.

3.3 Step 2. Multivariate Extreme Value Analysis

The flooding probability (Eq. 1) is computed via a Monte-Carlo sampling approach based on the random generation of the offshore conditions. To do so, two classes of offshore conditions are considered: 'amplitude' random variables $\mathbf{X}$=(*SWL*, *Hs*, *U*), which can take up very large values, and covariates $\mathbf{X}_c$=(T*p*, *Dp*, *Du*), which are dependent on the values of the 'amplitude' variables. Considering 'amplitude' variables, a multivariate extreme value analysis (Coles, 2001) is conducted to extrapolate their joint probability density to extreme values by taking into account the dependence structure. A three-step approach is performed:

Step (1) Fitting of the marginals of 'amplitude' variables through the combination of the empirical distribution, below a suitable high threshold *u*, and of the Generalised Pareto distribution (GPD) above the selected threshold *u* (Coles and Tawn, 1991) using the method of moments. Note that the marginal of *SWL* is estimated by combining the marginal of the skew surge with the empirical probability distribution of tides by following the convolution approach of Simon (1994). The threshold value *u* is selected using a combination of methods (visual inspection of quantile–quantile graphs, "mean residual life plots", "modified scale and shape parameters plots", see Coles, 2001);

Step (2) The dependence structure of the 'amplitude' variables is modelled using the approach of Heffernan and Tawn (2004). Let us denote $\widetilde{\mathbf{X}}_{-i}$ the vector of all variables (with prior transformation onto common standard Gumbel margins) except the ith variable X_i. A multivariate non-linear regression model is set up as follows:

$$\widetilde{\mathbf{X}}_{-i}|\{\tilde{X}_i = \tilde{x}_0\} = \boldsymbol{a}.\tilde{x}_0 + \tilde{x}_0^{\boldsymbol{b}}.\boldsymbol{W}, \qquad (4)$$

where $\tilde{x}_0 > \upsilon$ (i.e. $\tilde{X}_i$ having large values), $\boldsymbol{a}$ and $\boldsymbol{b}$ are parameters vectors (one value per parameter for each pair of variables), υ is a threshold that is selected using the diagnostic tools described in Heffernan and Tawn (2004: Sect. 4.4) and $\boldsymbol{W}$ is a vector of residuals. The model is adjusted using the maximum likelihood method assuming that the residuals $\boldsymbol{W}$ are Gaussian and independent of X_i with a mean and variance to be calculated. Once fitted, a Monte Carlo simulation procedure is used to randomly generate realisations of the 'amplitude' variables $\boldsymbol{X}$ (after transformation back on physical scales);

Step (3) Based on the generated dataset of amplitude variables, the random samples for the directional covariates *Dp* and *Du* are generated by using the empirical distribution conditional on the values of *H*s and of *U* respectively. The peak period T*p*

values are generated by following the approach described by Gouldby et al. (2014) based on a regression model using wave steepness conditional on Hs.

3.4 Step 3. Global Sensitivity Analysis and Shapley effect

The objective is to investigate the influence of the offshore conditions with respect to the occurrence of the event $\{m_Y > Y_C\}$ in relation to the flooding probability defined in Eq. 1. To do so, we opt for the GSA approach based on the Shapley effects proposed by Idrissi et al. (2021) and applied in the field of reliability assessment. For sake of presentation clarity, we first present the Shapley effect by considering the current situation where the variable of interest is a scalar variable (Sect. 3.4.1). Second, we present the adaptation in relation to the problem of flooding probability (Sect. 3.4.2).

3.4.1 Shapley effect for a scalar variable of interest

Among all the GSA methods (Iooss and Lemaitre, 2015), we opt for a variance-based GSA, denoted VBSA (Saltelli et al., 2008), which aims to decompose the total variance of the scalar variable of interest denoted here Z into the respective contributions of each uncertainty; this percentage being a measure of sensitivity.

Recall that f(.) is the numerical simulator. Consider the k-dimensional vector **x** as a random vector of k random input variables X_i (i=1,2,…,k) related to the different offshore forcing conditions. Then, the variable of interest Z=f(**x**) is also a random variable (as a function of a random vector). VBSA determines the part of the total unconditional variance $\mathrm{Var}(Z)$ of the output Z resulting from each input random variable X_i. Formally, VBSA relies on the first-order Sobol' indices (ranging between 0 and 1), which can be defined as:

$$S_i = \frac{\mathrm{Var}\big(\mathrm{E}(Z|X_i)\big)}{\mathrm{Var}(Z)},$$ (5)

where E(.) is the expectation operator.

When the input variables are independent, the index S_i corresponds to the main effect of X_i, i.e. the share of variance of Y that is due to a given X_i. The higher the influence of X_i, the lower the variance when fixing X_i to a constant value, hence the closer S_i to one.

When dependence/correlation exists among the input variables (as it is the case in our study, see Sect. 2.2), a more careful interpretation of Eq. 5 should be given: in this situation, a part of the sensitivity of all the other input variables correlated with the considered variable contributes to S_i, which cannot be interpreted as the proportion of variance reduction related to fixing X_i. To overcome this difficulty, an extension of the Sobol' indices have been proposed in the literature, namely the Shapley effects (Owen, 2014; Iooss and Prieur, 2019; Song et al., 2016). The advantage of these effects is to allocate a percentage of the model output's variance to each input variable which includes not only the individual effect, but also the higher-order interaction and above all, the (statistical) dependence. By summing to the total variance (i.e. the sum of all normalized effects is one) and by being non-negative, the Shapley effects allow for an easy interpretation (Iooss and Prieur, 2019).

Formally, the sensitivity indices are defined based on the Shapley value (Shapley, 1953) that is used in game theory to evaluate the "fair share" of a player in a cooperative game, i.e. it is used to fairly distribute both gains and costs to multiple players working cooperatively. Formally, a k-player game with the set of players $K=\{1,2,…,k\}$ is defined as a real-valued function that maps a subset of K to its corresponding cost $c: 2^K \rightarrow \mathbb{R}$ so that c(A) is the cost that arises when the players in the subset A of K participate in the game. The Shapley value of player i with respect to c(.) is defined as:

$$v_i = \frac{1}{k}\sum_{A \subseteq K \backslash \{i\}} \binom{k-1}{|A|}^{-1} (c(A \cup \{i\}) - c(A)),$$ (6)

where |A| is the size of the set A.

In the context of GSA, the set of players K can be seen as the set of inputs of f(.), and c(.) can be defined so that for $A \subseteq K$, c(A) measures the variance of Z caused by the uncertainty of the inputs in A. Owen (2014) proposed the so-called "closed Sobol' indices" as the cost function:

$$c(A) = S_A^{closed} = \frac{\text{Var}(E(Z|X_A))}{\text{Var}(Z)},$$ (7)

where X_A is the subset of inputs selected by the indices in A, namely ($X_A = (X_i)_{i \in A}$).

The Shapley effect can thus be defined as:

$$Sh_i = \frac{1}{k} \sum_{A \subseteq K \setminus \{i\}} \binom{k-1}{|A|}^{-1} (S_{A \cup \{i\}}^{closed} - S_A^{closed}),$$ (8)

3.4.2 Shapley effect for the occurrence of a flooding event

In our study, the Shapley effect cannot be directly applied because we are not interested in the variance of a scalar variable (denoted Z in Sect. 3.4.1), but in the occurrence of an exceedance event in relation to the flooding probability defined in Eq. 1. Thus, we rely on the adaptation of the Shapley effect to this case, namely 'Target Shapley effects' proposed by Idrissi et al. (2021) as follows:

$$TSh_i = \frac{1}{k} \sum_{A \subseteq K \setminus \{i\}} \binom{k-1}{|A|}^{-1} (TS_{A \cup \{i\}} - TS_A),$$ (9)

where $TS_A = \frac{\text{Var}(E(I_{\{m_Y > Y_C\}})|X_A)}{\text{Var}(I_{\{m_Y > Y_C\}})}$

The Target Shapley effects TSh_i can be interpreted as a percentage of the variance of the indicator function allocated to the input X_i, and measures the influence of the input to the occurrence of the flooding event (defined by the exceedance of the median value m_Y of Y above Y_C).

3.5 Estimation procedure

In practice, the Shapley effects defined in Eq. 9 are evaluated using a "given data" approach, i.e. through the post-processing of the Monte-Carlo-based results using the nearest neighbor search-based estimator developed by Broto et al. (2020) with the *sobolshap_knn* function of the R package *sensitivity*[1] using 5 neighbors and a pre-whitening of the inputs with the ZCA-cor procedure (Kessy et al., 2018).

In this estimation, two major sources of uncertainty should be accounted for, namely the Monte-Carlo sampling and the GP error (related to the approximation of the true numerical model by a GP built using a finite number of simulation results). This is done as follows:

Step (1) a set of N random realisations of the forcing conditions are generated using the methods described in Sect. 3.3;

Step (2) for the N randomly generated forcing conditions, a conditional (stochastic) N-dimensional simulation of the GP (knowing the training data) is generated using Eq. 2a and 2b, and the N values of m_Y are estimated;

Step (3) using the set of N values of m_Y, the flooding probability is estimated using Eq. 1 and the Shapley effects are computed using the nearest neighbor search-based estimator.

---

[1] https://cran.r-project.org/web/packages/sensitivity/sensitivity.pdf

Steps (1) to (3) are repeated B times to generate a set of B Shapley effects (one effect per forcing condition). The variability
315   in these estimates then reflects the use of different sets of random samples (sampling error) and the use of different conditional
simulations of the GP (GP error).

4 Application

In this section, we apply the procedure described in Sect. 3 to partition the uncertainty in the occurrence of the event $\{m_Y > Y_C\}$
by considering a base (reference) case defined by a volume threshold Y_C=2,000 m^3 which corresponds to a flooding event of
320   moderate magnitude (see Fig. 2b), and by the effect of *SLR* for RCP4.5 scenario (see Fig. 4b). The latter RCP scenario is
selected because it approximately corresponds to the Intended Nationally Determined Contributions submitted in 2015 ahead
of the Paris Agreement approval[2]. The impact of these assumptions is further discussed in Sect. 5.

4.1 Step 1. GP metamodel training and validation

Using the approach described in Sect. 3.2, we first select 100 offshore conditions used as inputs to the modelling chain to
325   calculate the corresponding median value m_Y (filled blue circles in Fig. 3). In addition, 44 extra cases (open blue circles in
Fig. 3) were defined using the set of high tide conditions that were randomly generated for the design of the early-warning
system at Gâvres (Idier et al., 2021: Sect. 2.5). These conditions were used as inputs of the metamodel implemented by Rohmer
et al. (2020) to predict the flooding-induced water height at the observation point P (Fig. 1b), which is a critical location with
respect to sea water entry during a storm event; the conditions leading to a positive water height were then selected. In total,
330   n=144 computer experiments were performed.

The GP model is trained by assuming a linear trend μ and a Matérn 5/2 kernel model in Eq. 2a,b and using a maximum
likelihood estimation of the GP parameters (e.g. Roustant et al., 2012). The GP metamodel is validated using a 10-fold cross
validation procedure as described in Sect. 3.2. Due to the highly skew distribution of m_Y, we use a logarithm transformation
i.e. $\log_{10}(m_Y + 1)$. The cross-validation, procedure shows a high predictive capability of the trained metamodel with
335    $Q^2 \approx 99.2\%$. Our preliminary tests also showed that the logarithm transformation improved the predictive capability with an
increase of Q^2 by 10%. The scatterplot in Fig. 6 confirms that the predictive capability of the trained GP model is very
satisfactory (the dots almost align along the first bisector). However, we can notice some deviations; in particular in the vicinity
of the volume threshold defining minor flooding event i.e. $\log_{10}(50+1) \approx 1.7$. This provides a clear justification for accounting
for the GP error in the GSA results by following the procedure described in Sect. 3.5.

[2]   https://unfccc.int/process-and-meetings/the-paris-agreement/nationally-determined-contributions-ndcs/nationally-determined-contributions-ndcs

340
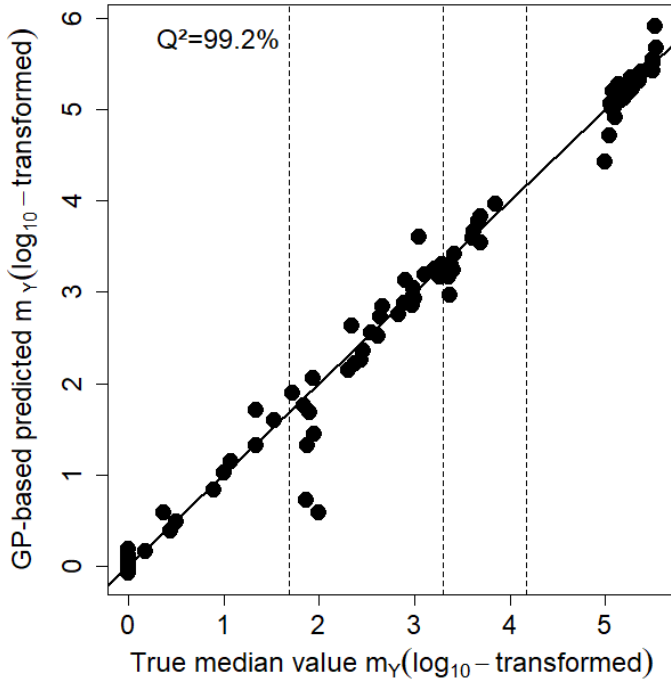
Figure 6: Comparison between the volume (log₁₀-transformed) estimated using the "true" numerical simulator and the ones predicted using the GP model based on a 10-fold cross-validation procedure. The closer the dots to the first bisector, the more satisfactory the predictive capability of the trained GP model. The performance indictor Q^2 is indicated and reaches here ~99.2%. The vertical dashed lines indicate the threshold Y_C (log₁₀-transformed) used in the study (50, 2,000 and 15,000 m³).

345 **4.2 Step 2. Multivariate Extreme value analysis**

We use the database of hindcast conditions described in Sect. 2.2 to extract >80,000 offshore forcing conditions characterized by the sixplets (*SWL, Hs, U, Tp, Dp,* and *Du*) taken at the time instant of the high tide (black dots in Fig. 3). Following Step (1) described in Sect. 3.3, the extracted data are used to fit the marginals of the 'amplitude' variables using the GPD distribution with the selected threshold value u_{Hs}=6.2m, $u_{Skew Surge}$=0.48m, and u_U=18.9m/s corresponding to ~2 extreme events / year. The

350 marginal distributions are provided in Supplementary Materials B.

Following Step (2) in Sect. 3.3, the dependence is modelled with the selected threshold υ of Eq. (2) set up at 0.97 (expressed as a probability of non-exceedance). On this basis, the Monte Carlo simulation procedure described by Heffernan and Tawn (2004) is used to randomly generate N=50,000 events (representative of 1,000 years). Based on the generated dataset, the corresponding covariate values are also generated (Step (3) in Sect. 3.2). Fig. 3 provides an overview of the randomly generated

355 samples (red dots) for the 'amplitude' variables and for the covariates. Note that some delineations (on the bottom left hand corner) can be noticed, which results from the threshold-based procedure to model the probabilistic distributions (see Sect. 3.3).

The visual analysis of this figure confirms the moderate-to-large statistical dependence between the sampled forcing conditions (if they were independent, no structure would be noticed) with satisfactory reproduction of the structure of the observations

360 (black dots). The examination of the (*a,b*)-parameters of the dependence model (as defined in Eq. 4) indicates a non-negligible positive strength of dependence in the class of asymptotic independence (Supplementary Materials A) in agreement with the analysis made on the hindcast database (Sect. 2.2).

4.3 Step 3. Uncertainty partitioning over time

The N=50,000 randomly generated forcing conditions in addition to the random *SLR* time series (see some examples in Fig.

365 4) are used as inputs of the validated GP models to evaluate the time evolution of P_f for Y_C=2,000m3 given RCP4.5 (Fig. 7). Preliminary convergence analysis showed that 50,000 Monte-Carlo samples were sufficient to reach stable results; this is also shown by the very small uncertainty band's width in Fig. 7 (see in particular the inserted plot) defined by the lower and upper

bounds computed using B=50 replicates of the estimation procedure (described in Sect. 3.5). Fig. 7 shows that P_f increases over time in a non-linear manner and reaches values of 10% in the long term, by 2100 and ~44% in the very long term, by 2200, i.e. equivalent to a return period (inverse of P_f) of respectively 10 years and about 2.3 years.
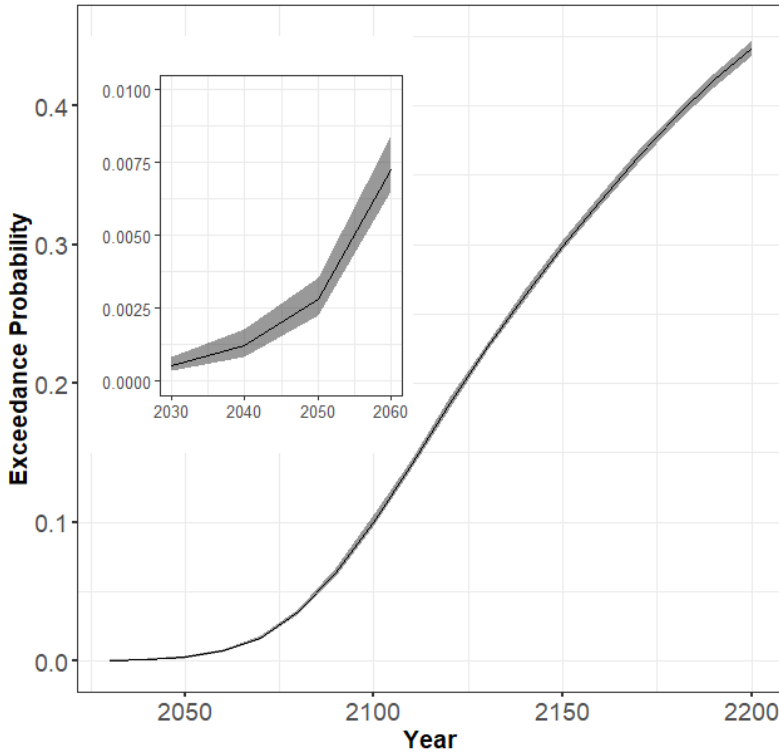
Figure 7: Time evolution of the probability of the event $\{m_Y > Y_C = 2,000 \text{m}^3\}$ **given** *SLR* **projections for the scenario RCP4.5. The inserted figure indicates the very small uncertainty band's width whose limits are the lower and upper bounds computed using B=50 replicates of the estimation procedure (Sect. 3.5) accounting for GP and sampling error.**

The Shapley effects for the flooding event $\{m_Y > 2,000 \text{m3}\}$ were evaluated using the 50,000 GP model evaluations using B=50 replicates of the estimation procedure (Sect. 3.5) accounting for GP and sampling error. Preliminary convergence analysis showed us that 50,000 samples were sufficient to reach low uncertainty estimates as shown at given time instants in Table 1. This also confirms that both error sources (GP and sampling) have small influence. Fig. 8 depicts the time evolution of the Shapley effects, which measure the influence of the inputs on the occurrence of the flooding event.
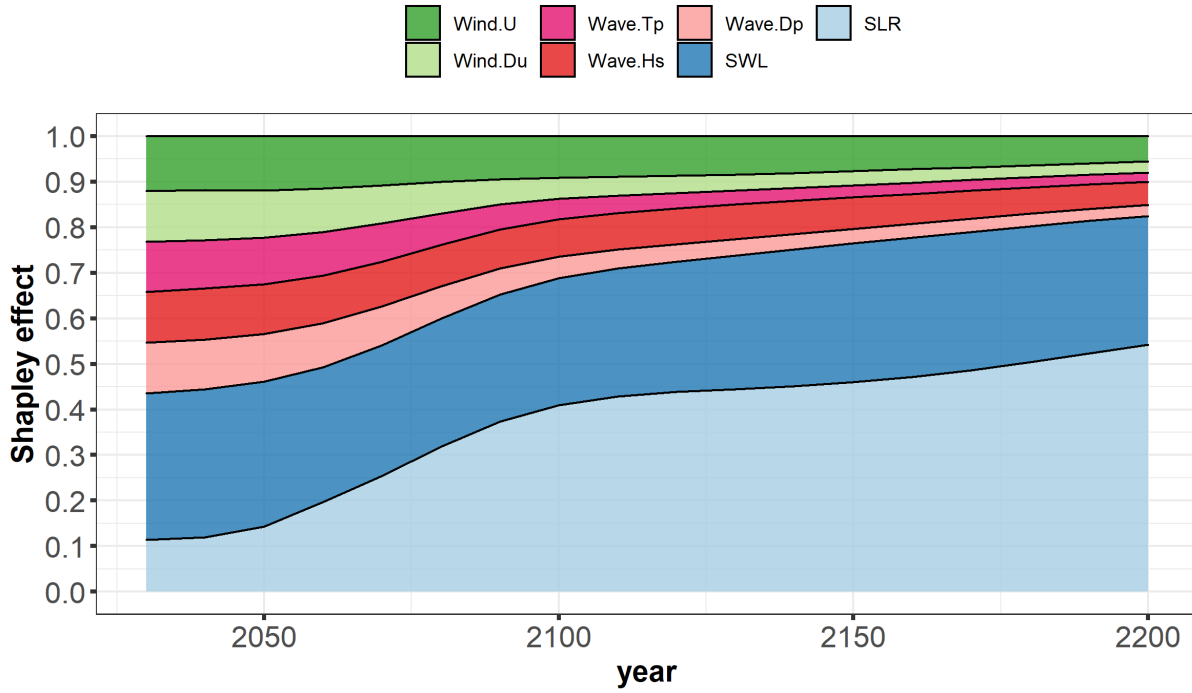
Figure 8: Time evolution of the Shapley effects, relative to the occurrence of the event $\{m_Y > Y_C = 2,000\text{m}^3\}$ given *SLR* projections for the scenario RCP4.5, estimated by computing the median value from B=50 replicates of the estimation procedure (Sect. 3.5) accounting for GP and sampling error.

Table 1. Shapley effects relative to the occurrence of the event $\{m_Y > Y_C = 2,000\text{m}^3\}$ given SLR projections for the scenario
385 **RCP4.5, estimated by computing the median value from B=50 replicates of the estimation procedure (Sect. 3.5) accounting for GP and sampling error. The numbers in brackets correspond to the minimum and maximum value computed from the B=50 replicates.**

Year	*SLR*	*SWL*	*Hs*	*Tp*	*Dp*	*U*	*Du*
2050	0.143 [0.126, 0.160]	0.319 [0.293, 0.344]	0.110 [0.095, 0.125]	0.102 [0.086, 0.119]	0.104 [0.095, 0.115]	0.119 [0.104,0.130]	0.104 [0.091, 0.112]
2100	0.410 [0.398, 0.420]	0.279 [0.270,0.291]	0.082 [0.078, 0.085]	0.045 [0.043, 0.047]	0.047 [0.044, 0.051]	0.091 [0.086, 0.096]	0.047 [0.044, 0.050]
2200	0.542 [0.536, 0.550]	0.282 [0.277, 0.286]	0.050 [0.048, 0.053]	0.020 [0.019, 0.022]	0.025 [0.022, 0.027]	0.056 [0.053, 0.059]	0.024 [0.022, 0.025]

Several effects are noticed:

- The influence of *SLR* increases over time with a non-negligible contribution of ~15% even in the short term (<2050)
390 until reaching ~40% in the long term (2100) by following a relatively steep evolution (with an increase by 180% from 2020 to 2100);

- After 2100, *SLR* contribution continues to increase until reaching ~55% in the very long term (2200) but by following a relatively gentle linear evolution (with an increase by 37.5% over a 100-year time duration from 2100 to 2200). This means that by 2200, *SLR* dominates the cumulative contributions of all remaining uncertainties;

395 - In the short term, the major contributor corresponds to *SWL*. The Shapley effect is of ~32%, while the remaining forcing conditions have contributions of the order of 10-13%. We also note that by 2080, *SLR* Shapley effect exceeds the one of *SWL*;

- Over time, the contributions of all forcing conditions (except *SLR*) decrease (to compensate the *SLR* increase because the sum of all Shapley effects is one) until reaching a quasi-horizontal plateau by 2100. The Shapley effects are of the order of 28% for *SWL* and 8-9% for *H*s and *U*, hence indicating their small-to-moderate influence though non-negligible;

- The Shapley effects of the covariates (*D*p, *T*p and *D*u) reach however low values <3-4%, which provides a strong evidence of their negligible role for time horizon >2100, i.e. their individual effect as well as their dependence and their interactions with the other variables are almost zero. This effect would not have been revealed if 'traditional' sensitivity analysis (using Sobol' indices) had been used, because the strong dependence among the inputs would not have been accounted for (Supplementary Materials C).

5 Discussion

In this section, we first investigate whether the conclusions on the uncertainty partitioning (Sect. 4.3) might change depending on some key modelling choices (Sect. 5.1). Second, we further discuss the implications of different limitations for both the numerical and the statistical modelling (Sect. 5.2).

5.1 Influence of key modelling choices

The uncertainty partitioning in Sect. 4.3 underlines the key influence of *SLR* on the occurrence of the event $\{m_Y > Y_C = 2,000\text{m}^3\}$. We investigate here to which extent alternative assumptions underlying our approach might change the afore-described conclusions, namely:

- the volume threshold Y_C used to define when a flooding event occurs: the analysis was performed given a threshold Y_C=2,000m^3 related to a moderate flooding event (Fig. 2), and it is re-conducted here by respectively focusing on minor and very large flooding events defined for Y_C=50 and 15,000m^3 (as illustrated in Fig. 2);

- the choice in the RCP scenario to constrain the *SLR* projections described in Sect. 2.3: the analysis was conducted given the RCP4.5 scenario i.e. given a scenario related to relatively moderate *SLR* magnitude (Fig. 4b), compared to RCP8.5 in particular (Fig. 4c). The analysis is here re-conducted for the RCP2.6 and 8.5 scenarios;

- the choice of the DEM: this modelling choice is known to highly influence the results (see e.g., Abily et al., 2016), and we investigate to which extent an alternative DEM might change the sensitivity analysis results by considering the DEM 2008 (with the same resolution of 3m as DEM 2015), which corresponds to the conditions before the major flooding event of Johanna 2008 i.e. prior to the protectives measures relying on the raise of the dykes in the aftermath of this event;

- the choice of the summary statistics to account for wave stochasticity: the analysis was conducted by using the median value m_Y of *Y* as described in Sect. 2.1. The analysis is here re-conducted using the 1st quartile (denoted Q_{25}), or the 3rd quartile (denoted Q_{75}).

For each analysis, the corresponding assumption was changed and the whole analysis (described in Sect. 3.1) was re-conducted, i.e. (1) new hydrodynamic simulations; (2) training of new GP models (the predictive capability is confirmed as shown in Supplementary Materials E); (3) GP-based estimate of the flooding probability and of the Shapley effects within a Monte-Carlo-based simulation procedure (Sect. 3.5).
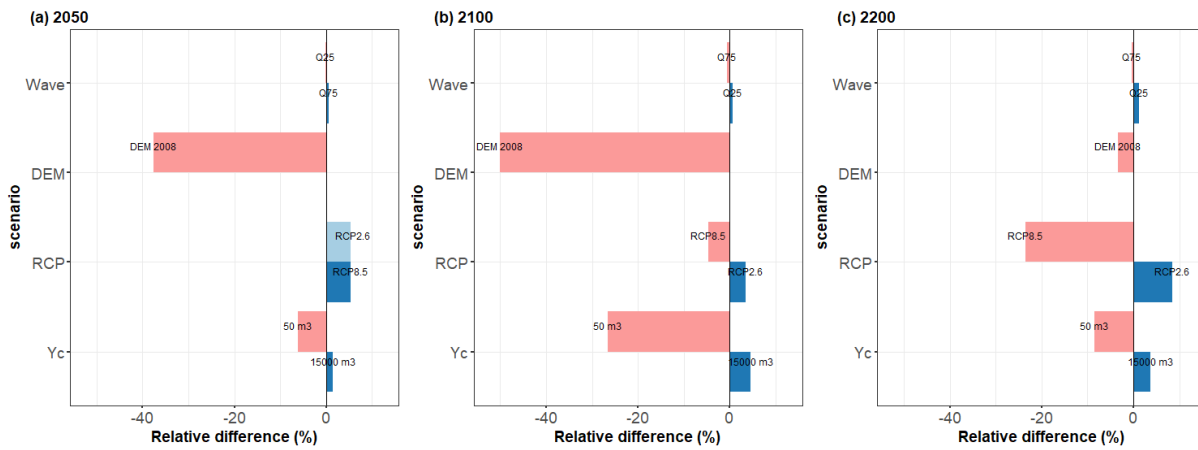
Figure 9: Relative differences of the Shapley effect for *SLR* (using the median value computed for B=50 replicates of the estimation procedure) with respect to the base case at different time horizons (2050 (a), 2100 (b) and 2200 (c)) considering alternatives modelling choices for the volume threshold Y_C, the RCP scenario, DEM and the summary statistics of wave stochasticity.

Figure 9 summarizes these results and shows that the *SLR* effect both depends on our modelling choices and on the considered time horizon. Before 2100, it is strongly influenced by the DEM (Fig. 9a,b). The differences in the short/long term were expected because DEM 2008 presents some sectors of lower topographic elevation of coastal defences (Supplementary Materials D) compared to DEM 2015 (in particular on the south-eastern sector, which is highly exposed to storm impacts). A more detailed analysis of the uncertainty contribution (Supplementary Materials E) shows that the decrease of *SLR* influence for DEM 2008 goes in parallel with higher contributions of wave characteristics, hence confirming that drivers of flooding change depending on the DEM; the sectors with lower topographic elevation having a higher sensitivity to wave-induced flooding, i.e. overtopping at least until 2100.

In the long term (beyond 2100), the threshold importance becomes significant (Fig. 9b). Case Y_C=50m3 presents a slower increase of *SLR* influence, which is directly translated into a slower reduction of *SWL* contribution (Supplementary Materials E). This *SLR*-threshold relation directly reflects how *SLR* acts on the flooding likelihood: it acts as an "offset", which means that it induces a higher sea water level at the coast; hence a higher likelihood of flooding. Thus, the lower the threshold value, the lower the necessary *SLR* magnitude to induce flooding, hence the lower influence. This threshold also means that results presented in Fig. 8 are specific to our case study in Gâvres. In other settings where flooding is dominated by overflow, breaching or overtopping with another threshold, the partition of uncertainties is expected to be different.

It is only in the very long term (beyond 2100) that the RCP scenario starts to play a key role on *SLR* influence. This effect is related to the similarity in sea level projections across climate scenarios until the mid-21st century (Fox-Kemper et al., 2021). Like for Y_C, this is the "offset" effect of *SLR* that influences the most: for RCP8.5, the mode of the *SLR* distribution (in red in Fig. 4c) exceeds the one of the other scenarios after 2100, and can induce a high sea water level at the coast, hence potentially a water volume value close to Y_C=2,000 m³, and a higher flooding likelihood. This means that *SLR* values sampled around the mode will less impact the occurrence of the flooding event (and the flooding probability), because a small *SLR* offset is here necessary to trigger the flooding event. This is not the case for the two alternative RCP scenarios, because the mode is of lower magnitude and any *SLR* values sampled above it will have a key impact on the flooding occurrence.

Finally, the uncertainty partitioning is shown to be very little influenced by the choice of the summary statistics for the wave stochasticity (Fig. 9) whatever the time horizon. This result differs from the one of Idier et al. (2020b), who showed the importance of this effect that was there comparable to the one of *SLR* as long as the still water level remains smaller than the critical level above which overflow occurs. The differences between both studies may be explained by the differences in the procedure. Idier et al. (2020b) analysed this effect for two specific past storm events, whereas our study covers a large number of events by randomly sampling different offshore forcing conditions. To conclude on this effect (relative to the others), further investigations are thus necessary and could benefit for instance from recent GSA for stochastic simulators (Zhu and Sudret, 2021).

5.2 Limitations

While the analysis in Sect. 5.1 covers the main modelling choices of our procedure, we acknowledge that several aspects
470   deserve further improvements.

Regarding the modelling of the flood processes, one of our main assumptions is to perform simulations with steady state offshore forcing conditions, i.e. without accounting for the time evolution of the forcing conditions around the high tide (Sect. 2.1). First, this choice was guided by the computational budget that could be afforded to account for wave stochasticity via repeated numerical simulations. A total of 144×20=2,880 numerical simulations were performed here for our analysis: such a
475   large number of simulations would be difficult to achieve using non-stationary numerical simulations, because a single run takes about 3 days of computation on 48 cores. Second, Idier et al. (2020b) showed, on two historical storm events, that the value of Y remains of the same order of magnitude between a steady-state and a non-stationary simulation. Therefore, the temporal effect is expected to influence only moderately our conclusions regarding uncertainty partitioning. If, however, other flooding indicators are chosen (e.g. total flooded area, or water height at a given inland location), i.e. indicators that are more
480   sensitive to the time evolution of offshore conditions, non-stationary simulations are mandatory. In this case, time dimension should be accounted for at different levels of the procedure: (1) metamodelling with functional inputs (e.g. using the procedure developed by Betancourt et al., 2020); (2) integrating additional variables in the multivariate extreme value analysis like event duration and event spacing (e.g. Callaghan et al., 2008); (3) random generation of time-varying forcing conditions (e.g. using the stochastic emulator used by Cagigal et al. (2020) to force ensemble long-term shoreline predictions).

485   Regarding the physical drivers of flooding, the analysis was focused on marine flooding by considering the joint effects of wave-wind-sea level, but additional processes are also expected to play a role in driving the compound flooding, like river discharge (in particular with the proximity of the Blavet river[3] on the study area) or rainfall. Including additional drivers is made here feasible by the flexibility of Heffernan and Tawn (2004)'s approach for analysing high dimensional extremes. This was shown in particular by Jane et al. (2020), who also highlighted the value of copula-based approaches, such as Vine copula.
490   An avenue for future research could include the comparison of different approaches for multivariate extreme value analysis, i.e. a type of modelling uncertainty on top of the uncertainties in the parametrization and in the threshold selection of these techniques (e.g. Northrop et al., 2017).

Finally, regarding the drivers' evolution under climate change, we used the projections from Kopp et al. (2014). These are generally consistent with the latest IPCC sea-level projections presented in the Special Report on Ocean and Cryosphere in a
495   Changing Climate (Oppenheimer et al., 2019). The range of these projections is also similar with medium confidence projections provided by the 6th Assessment report of IPCC, at least until 2100 (Fox-Kemper et al., 2021). Yet, the highest quantiles may not represent well the possibility of marine ice-sheet collapse in Antarctica (De Conto et al., 2021). The lowest quantiles of the Kopp et al. (2014)'s projections need to be considered even more cautiously, the 17% quantile being a reasonable minimal estimate (named low-end scenario, see e.g. Le Cozannet et al., 2019b) given the scientific evidence
500   available today. Integrating these updated data is a line for future work whose implementation will benefit from the low computational budget of the metamodels. In addition, one of our main assumptions regarding SLR is that only SWL is impacted, while the current wave and wind climate remain unchanged in the future. This assumption should be reconsidered in future work in particular in the light of recent projections (see e.g. Morim et al. (2020) for wave and Outten and Sobolowski (2021) for wind) and by taking advantages of recent advances in stochastic modelling like the one used by Cagigal et al. (2020).

---

[3]   See   Blavet   gauge   measurements   (in   French),   https://www.vigicrues.gouv.fr/niv3-station.php?CdEntVigiCru=8&CdStationHydro=J571211004&GrdSerie=H&ZoomInitial=3

6 Concluding remarks

At the macrotidal site of Gâvres (French Britany), we have estimated the time evolution of the flooding probability defined so that the median value m_Y (related to wave stochasticity) of the inland water volume Y induced by the flooding exceeds a given threshold Y_C. For moderate flooding events (with Y_C=2,000m3), the flooding probability rapidly reaches ~10% (return period of 10 years) by 2100 and (quasi-)linearly increases until ~44% (~2.3years) in the very long term (by 2200). By relying on Shapley effects, our study underlines the key influence of SLR on the occurrence of the event $\{m_Y > Y_C\}$ regardless of Y_C value together with a small-to-moderate contribution of wave and of wind characteristics and even of negligible importance in the very long term for the covariates, Dp, Du and Tp. This growing influence of SLR (and then of the climate scenarios over the 21st and 22nd centuries) was expected, and is a feature that would be observed across many coastal sites in the world. Yet, the time evolution of the flood probability (and associated uncertainty) remains site-specific, i.e. mostly related to the particular conditions that generate flooding in each coastal area, and could not have been quantified without the implementation of the proposed procedure.

The analysis of the main uncertainties in the estimation procedure (Monte-Carlo sampling and GP error) shows here minor impact, which is a strong indication that the combined GP-Shapley effect approach is a robust tool worth integrating in the toolbox of coastal engineers and managers to explore and characterize uncertainties related to compound coastal flooding under SLR. However, to reach an operative level, two key aspects deserve further investigation: (1) the optimized computational effort with appropriate metamodelling techniques (e.g. Betancourt et al. (2020) for functional inputs, Zhu and Sudret (2021) for stochastic simulators) combined with advanced Monte-Carlo sampling scheme (like importance sampling, Demange-Chryst et al. (2022)); (2) the capability to assess the impact of alternative modelling choices (extreme value modelling, numerical modelling, in addition to those described in Sect. 5.1) on the sensitivity analysis, i.e. a problem named 'sensitivity analysis of sensitivity analysis' by Razavi et al. (2021). This latter aspect requires a more general framework to incorporate multiple levels of uncertainty, i.e. a first level that corresponds to the forcing conditions, a second level that is related to the modelling choices and a third level that is related to the stochastic nature of our numerical model (related to wave stochasticity).

Author contributions

JR, DI and GLC designed the concept. JR, DI and FB set up the methods. JR, DI, RT, GLC, and FB set up the numerical experiments. DI performed the numerical analyses with the hydrodynamic model. RT and GLC pre-processed and provided the projection data. JR undertook the statistical analyses. JR wrote the manuscript draft, DI, RT, GLC and FB reviewed and edited the manuscript.

Competing interests

The authors declare that they have no conflict of interest.

Code/Data availability

Codes are available upon request to the first author.

Acknowledgements

The authors thank the ANR for its financial support to the RISCOPE project (ANR-16-CE04-0011). We thank F. Gamboa (IMT), T. Klein (IMT/ENAC), and R. Pedreros (BRGM) for fruitful discussions.

References

Abily, M., Bertrand, N., Delestre, O., Gourbesville, P., and Duluc, C. M.: Spatial Global Sensitivity Analysis of High Resolution classified topographic data use in 2D urban flood modelling. Environmental Modelling & Software, 77, 183-195, 2016.

Anderson, B., Borgonovo, E., Galeotti, M., and Roson, R.: Uncertainty in climate change modelling: can global sensitivity analysis be of help?, Risk analysis 2014, 34(2), 271-293, 2014.

Athanasiou, P., van Dongeren, A., Giardino, A., Vousdoukas, M.I., Ranasinghe, R., and Kwadijk, J.: Uncertainties in projections of sandy beach erosion due to sea level rise: an analysis at the European scale. Sci. Rep., 10, 11895, 2020.

Ardhuin, F., Rogers, W.E., Babanin, A.V., Filipot, J., Magne, R., Roland, A., Van der Westhuysen, A., Queffeulou, P., Lefevre, J., Aouf, L., and Collard, F.: Semiempirical dissipation source functions for ocean waves. Part I: Definition, calibration, and validation, J. Phys. Oceanogr., 40(1), 917-941, 2010.

Bamber, J. L., and Aspinall, W. P.: An expert judgement assessment of future sea level rise from the ice sheets, Nat. Clim. Chang., 3, 424–427, 2013.

Betancourt, J.; Bachoc, F.; Klein, T.; Idier, D.; Pedreros, R.; and Rohmer, J.: Gaussian process metamodeling of functional-input code for coastal flood hazard assessment. Reliability Engineering & System Safety, 198, 106870, 2020.

Bevacqua, E., Vousdoukas, M. I., Zappa, G., Hodges, K., Shepherd, T. G., Maraun, D., Mentaschi, L., and Feyen, L.: More meteorological events that drive compound coastal flooding are projected under climate change. Communications earth & environment, 1(1), 1-11, 2020.

Broto, B., Bachoc, F., and Depecker, M.: Variance reduction for estimation of Shapley effects and adaptation to unknown input distribution, SIAM/ASA Journal of Uncertainty Quantification, 8, 693-716, 2020.

Cagigal, L., Rueda, A., Anderson, D.L., Ruggiero, P., Merrifield, M.A., Montaño, J., Coco, G., and Méndez, F.J.: A multivariate, stochastic, climate-based wave emulator for shoreline change modelling. Ocean Model. 154, 2020.

Callaghan, D. P., Nielsen, P., Short, A., and Ranasinghe, R.W.M.R.J.B.: Statistical simulation of wave climate and extreme beach erosion. Coastal Engineering, 55(5), 375-390, 2008.

Chaumillon, E., Bertin, X., Fortunato, A. B., Bajo, M., Schneider, J. L., Dezileau, L., et al.: Storm-induced marine flooding: Lessons from a multidisciplinary approach. Earth-Science Reviews, 165, 151-184, 2017.

Coles, S.: An Introduction to Statistical Modeling of Extreme Values, Springer Verlag, London, 2001.

Coles, S., J. Heffernan, and J. Tawn: Dependence Measures for Extreme Value Analyses. Extremes 2:4, 339–365, 1999.

Coles, S.G., Tawn, J.A.: Modelling extreme multivariate events, J. R. Stat. Soc. Ser. B Methodol., 53(2), 377–392, 1991.

De Conto, R.M., Pollard, D., Alley, R.B., Velicogna, I., Gasson, E., Gomez, N., Sadai, S., Condron, A., Gilford, D.M., Ashe, E.L. and Kopp, R.E.: The Paris Climate Agreement and future sea-level rise from Antarctica. Nature, 593(7857), 83-89, 2021.

Demange-Chryst, J., Bachoc, F., and Morio, J.: Shapley effect estimation in reliability-oriented sensitivity analysis with correlated inputs by importance sampling, 2022, arXiv preprint arXiv:2202.12679.

Do, N. C., and Razavi, S.: Correlation effects? A major but often neglected component in sensitivity and uncertainty analysis. Water Resources Research, 56(3), e2019WR025436, 2020.

Fox-Kemper, B., Hewitt, H.T., Xiao, C., Aðalgeirsdóttir, G., Drijfhout, S.S., Edwards, T.L., et al.: Ocean, Cryosphere and Sea Level Change. In Climate Change 2021: The Physical Science Basis. Contribution of Working Group I to the Sixth Assessment Report of the Intergovernmental Panel on Climate Change [MassonDelmotte, V.,P. Zhai, A. Pirani, S.L. Connors, C. Péan, S. Berger, N. Caud, Y. Chen, L. Goldfarb, M.I. Gomis, M. Huang, K. Leitzell, E. Lonnoy, J.B.R. Matthews, T.K. Maycock, T. Waterfield, O. Yelekçi, R. Yu, and B. Zhou (eds.)]. Cambridge University Press. In Press, 2021.

Gouldby, B., Méndez, F. J., Guanche, Y., Rueda, A., and Mínguez, R.: A methodology for deriving extreme nearshore sea conditions for structural design and flood risk analysis, Coastal Engineering, 88, 15-26, 2014.

Heffernan, J.E., and Tawn, J.A.: A conditional approach for multivariate extreme values (with discussion), J. R. Stat. Soc. Ser. B Stat. Methodol., 66(3), 497–546, 2004.

585 Kessy, A., Lewin, A., and Strimmer, K.: Optimal whitening and decorrelation, The American Statistician, 72(4), 309-314, 2018.

Idier, D., Rohmer, J., Pedreros, R., Le Roy, S., Lambert, J., Louisor, J., Le Cozannet, G., and Le Cornec, E.: Coastal flood: a composite method for past events characterisation providing insights in past, present and future hazards—joining historical, statistical and modelling approaches, Natural Hazards, 101(2), 465-501, 2020a.

590 Idier, D., Pedreros, R., Rohmer, J., and Le Cozannet, G.: The effect of stochasticity of waves on coastal flood and its variations with sea-level rise, Journal of Marine Science and Engineering, 8(10), 798, 2020b.

Idier, D., Aurouet, A., Bachoc, F., Baills, A., Betancourt, J., Gamboa, F., et al.: A User-Oriented Local Coastal Flooding Early Warning System Using Metamodelling Techniques. Journal of Marine Science and Engineering, 9(11), 1191, 2021.

Idrissi, M. I., Chabridon, V., and Iooss, B.: Developments and applications of Shapley effects to reliability-oriented sensitivity
595 analysis with correlated inputs, Environmental Modelling & Software, 143, 105115, 2021.

Iooss, B., and Lemaître, P. (2015). A review on global sensitivity analysis methods, in: Uncertainty management in simulation-optimization of complex systems, edited by Dellino, G., and Meloni, C., Springer, Boston, MA, 101-122, 2015.

Iooss, B., and Prieur, C.: Shapley effects for Sensitivity Analysis with correlated inputs: Comparisons with Sobol' Indices, Numerical Estimation and Applications, International Journal for Uncertainty Quantification, 9(5), 493-514, 2019.

600 Jane, R., Cadavid, L., Obeysekera, J., and Wahl, T.: Multivariate statistical modelling of the drivers of compound flood events in south Florida. Natural Hazards and Earth System Sciences, 20(10), 2681-2699, 2020.

Le Cornec, E., Le Bris, E., and Van Lierde, M.: Atlas des risques littoraux sur le departement du Morbihan. Phase 1 : Recensement et consequences des tempetes et coups de vent majeurs. GEOS-AEL and DHI report (in French). 476 pp., 2012.

Le Cozannet, G.; Rohmer, J.; Cazenave, A.; Idier, D.; van De Wal, R.; De Winter, R., Pedreros, R., Balouin, Y., Vinchon, C.,
605 and Oliveros, C.: Evaluating uncertainties of future marine flooding occurrence as sea-level rises, Environmental Modelling & Software, 73, 44-56, 2015.

Le Cozannet, G., Bulteau, T., Castelle, B., Ranasinghe, R., Wöppelmann, G., Rohmer, J., Bernon, N., Idier, D., Louisor, J., and Salas-y-Mélia, D.: Quantifying uncertainties of sandy shoreline change projections as sea level rises, Scientific reports, 9(1), 1-11, 2019a.

610 Le Cozannet, G., Thiéblemont, R., Rohmer, J., Idier, D., Manceau, J.C. and Quique, R.: Low-end probabilistic sea-level projections. Water, 11(7), 1507, 2019b.

Marcos, M., Rohmer, J., Vousdoukas, M. I., Mentaschi, L., Le Cozannet, G., and Amores, A.: Increased extreme coastal water levels due to the combined action of storm surges and wind waves, Geophysical Research Letters, 46(8), 4356-4364, 2019.

Minasny, B., and McBratney, A. B.: A conditioned Latin hypercube method for sampling in the presence of ancillary
615 information. Computers & geosciences 32(9):1378-1388, 2006.

Morim, J., Trenham, C., Hemer, M., Wang, X.L., Mori, N., Casas-Prat, M., et al.: A global ensemble of ocean wave climate projections from CMIP5-driven models. Scientific data, 7(1), 1-10, 2020.

Northrop, P. J., Attalides, N., & Jonathan, P.: Cross-validatory extreme value threshold selection and uncertainty with application to ocean storm severity. Journal of the Royal Statistical Society: Series C (Applied Statistics), 66(1), 93-120, 2017.

620 Oppenheimer, M.; Glavovic, B.C.; Hinkel, J.; van de Wal, R.; Magnan, A.K.; Abd-Elgawad, A.; Cai, R.; Cifuentes-Jara, M.; DeConto, R.M.; Ghosh, T., et al.: Sea Level Rise and Implications for Low-Lying Islands, Coasts and Communities, in: Pörtner, H.-O. et al. (eds), IPCC Special Report on the Ocean and Cryosphere in a Changing Climate, Cambridge University Press, Cambridge, UK, 321-445, 2019.

Outten, S.; and Sobolowski, S: Extreme wind projections over Europe from the Euro-CORDEX regional climate models.
625 Weather and Climate Extremes, 33, 100363, 2021.

Owen, A. B.: Sobol' indices and Shapley value, SIAM/ASA Journal of Uncertainty Quantification, 2, 245-251, 2014.

Razavi, S., Jakeman, A., Saltelli, A., Prieur, C., Iooss, B., Borgonovo, E., et al.: The future of sensitivity analysis: an essential discipline for systems modeling and policy support, Environmental Modelling & Software, 137, 104954, 2021.

Rohmer, J., Idier, D., and Pedreros, R.: A nuanced quantile random forest approach for fast prediction of a stochastic marine flooding simulator applied to a macrotidal coastal site, Stochastic Environmental Research and Risk Assessment, 34(6), 867-890, 2020.

Roustant, O., Ginsbourger, D., and Deville, Y.: DiceKriging, DiceOptim: Two R packages for the analysis of computer experiments by kriging-based metamodeling and optimization, Journal of Statistical Software, 51(1), 1–55, 2012.

Saltelli, A., Ratto, M., Andres, T., Campolongo, F., Cariboni, J., Gatelli, D., Saisana, M., and Tarantola, S. (Eds.): Global sensitivity analysis: the primer, JohnWiley & Sons, 2008.

Shapley, L. S.: A value for n-person games, in: Contributions to the Theory of Games, edited by Kuhn, H., and Tucker, A. W., Volume II, Annals of Mathematics Studies, Princeton University Press, Princeton, NJ, 307-317, 1953.

Simon, B.: Statistique des niveaux marins extrêmes le long des côtes de France, SHOM 884 Report no. 001/94, 1994 (in French).

Song, E., Nelson, B., and Staum, J.: Shapley effects for global sensitivity analysis: Theory and computation, SIAM/ASA Journal on Uncertainty Quantification, 4 (1), 1060-1083, 2016.

Wahl, T., Jain, S., Bender, J., Meyers, S. D., and Luther, M. E.: Increasing risk of compound flooding from storm surge and rainfall for major US cities. Nature Climate Change, 5(12), 1093-1097, 2015.

Wahl, T., Haigh, I. D., Nicholls, R. J., Arns, A., Dangendorf, S., Hinkel, J., and Slangen, A. B.: Understanding extreme sea levels for broad-scale coastal impact and adaptation analysis, Nature communications, 8(1), 1-12, 2017.

Ward, P. J., Couasnon, A., Eilander, D., Haigh, I. D., Hendry, A., Muis, S., Veldkamp, T. I. E., Winsemius, H. C., and Wahl, T.: Dependence between high sea-level and high river discharge increases flood hazard in global deltas and estuaries. Environmental Research Letters, 13(8), 084012, 2018.

Williams, C. K., and Rasmussen, C. E.: Gaussian processes for machine learning, MIT press, Cambridge, MA, 2006.

Wong, T.E., and Keller, K.: Deep uncertainty surrounding coastal flood risk projections: A case study for New Orleans. Earth's Future 2017, 5(10), 1015-1026, 2017.

Zhu, X., and Sudret, B.: Global sensitivity analysis for stochastic simulators based on generalized lambda surrogate models, Reliability Engineering & System Safety, 107815, 2021.

Zijlema, M., Stelling, G., and Smit, P.: SWASH: An operational public domain code for simulating wave fields and rapidly varied flows in coastal waters, Coastal Engineering, 58(10), 992-1012, 2011.